Research Article Vol. 32, No. 4 / 12 Feb 2024 / Optics Express 6432
Optics EXPRESS

Tunable origami metastructure based on liquid crystal for curvature sensing

YI-QIANG BAO,[1] BING-XIANG LI,[1,2] AND HAI-FENG ZHANG[1,3]

[1]College of Electronic and Optical Engineering & College of Flexible Electronics (Future Technology), Nanjing University of Posts and Telecommunications, Nanjing 210023, China
[2]bxli@njupt.edu.cn
[3]hanlor@163.com

Abstract: In this paper, a liquid crystal (LC) tunable origami metastructure (OMS) designed for curvature sensing on cylindrical surfaces to measure their curvature is introduced. The LC employed is K15 (5CB) and the applicable band is 0.36~23 GHz. When excited by electromagnetic waves (EMWs) within the 4~16 GHz, the resonance frequency of the OMS shifts from 10.24 GHz to 10.144 GHz, corresponding to a change in absorption amplitude ranging from 0.773 to 0.920. In terms of curvature sensing, the detectable range of curvature spans from 0 to 0.327 mm^{-1}. The maximum sensitivity (S) achieved for curvature measurement reaches 0.918/mm^{-1}, accompanied by a quality factor (Q-factor) of 25.88. The proposed OMS embodies numerous excellent traits, including wide-range sensing capabilities and heightened S, promising for applications in bionic skin, smart robotics, and related fields.

1. Introduction

As research on bionic robots continues to advance, the application of sensors in this field has become increasingly extensive, encompassing curvature sensors (CSs), temperature sensors, vision sensors, and more. The CSs could provide bionic robots with the haptic feedback they require, enabling the sensing of bending in joints, fingers, and the spine [1]. This capability enables them to accurately perceive and comprehend the shape and structure of their surroundings, which is crucial for bionic robots to operate and interact effectively. At present, most of the CSs are fiber optic sensing and electrical sensors [2]. These sensors come with high installation costs, maintenance complexities, and poor performance. Therefore, it's imperative to explore cost-effective and user-friendly curvature sensor design alternatives.

Metastructure (MS) refers to an artificial electromagnetic microstructure meticulously designed to exert precise control and exhibit specific responses to electromagnetic waves at the microscopic level [3]. This tailored manipulation enables its application across various technological domains reliant on managing EMW behavior. MSs have extensive potential applications in wireless communication [4], invisibility cloaks [5], and detection [6]. In recent years, many new or improved sensor applications of MS have been proposed. Melik *et al.* designed a highly sensitive strain sensor based on MS, which is highly responsive to mechanical deformation. The surface strain of the material is measured through resonance frequency shifts [7]. Aristov *et al.* investigated the excitation of plasmon modes in 3D plasma crystal metamaterials, which provided exceptionally high spectral sensitivity [8]. Bakır *et al.* proposed an absorber-based MS sensor for pressure, temperature, density, and humidity sensing [9]. Lio *et al.* utilized epsilon near zero and Fano-Rabi physics to design a metamaterial system with ultra-high sensitivity [10]. Furthermore, the utilization of flexible MS presents an innovative and practical design approach for advancing CSs. In fact, sensor detection modes can be categorized into spectral detection and intensity detection as well [2]. Yang *et al.* developed a CS based on a fiber optic Mach Zehnder interference (MZI), which detects curvature by monitoring changes in intensity within the interference valleys [11]. Intensity detection presents several advantages, including real-time

#517881 https://doi.org/10.1364/OE.517881
Journal © 2024 Received 5 Jan 2024; revised 30 Jan 2024; accepted 30 Jan 2024; published 7 Feb 2024

Optics EXPRESS

monitoring, swift responsiveness, simplified equipment and operations, and cost-effectiveness. These attributes open up novel avenues for applying MSs in curvature sensing.

CSs require flexible and bendable substrate materials for their design. In 2021, inspired by the pangolin, Wang *et al.* developed a stretchable MS composed of resonance units and elastomers. This strategy can be seamlessly attached to curved surfaces, including spherical dome and saddle surfaces [12]. Moreover, there is extensive research on using paper-based materials (*e.g.*, Polyimide) as flexible substrates for MS [13], apart from flexible materials such as elastomers. Tomital *et al.* in 2023 proposed a paper-based MS for head protection, whereby the origami metastructure (OMS) will shape-compress from a bending pattern to cushion during an impact [14]. In practice, the OMS can be applied to the electromagnetic wave (EMW) field as well. In 2023, Han's team introduced a honeycomb absorber based on aramid fiber paper. This absorber features a traditional honeycomb origami structure and has an absorptivity bandwidth ranging from 3.6 to 18 GHz [15]. The bendable capability of paper-based materials offers more options for the design of curvature sensing structures.

Currently, two main categories of CSs are available: optic fiber (OF) sensors and electrical sensors. Among these, researchers often favor OF sensors for their advantages, such as small size, resistance to electromagnetic interference, and corrosion. Xiao *et al.* proposed and experimentally demonstrated a CS based on fiber MZI and microwave photonic filter, with a sensitivity of -147.634 MHz/m^{-1} [16]. Zhao *et al.* proposed and validated a novel curvature and temperature sensor based on off-axis high-order mode long-period fiber grating. The instantaneous curvature sensitivity can exceed 20 dB/m^{-1} [17]. Yin *et al.* proposed an intensity-modulated microstructured OF CS, achieving a sensitivity of 0.18 dB/m^{-1} [18]. Additionally, the design schemes of OF sensors with respect to curvature research include Fabry Pérot cavities [19], and upconversion luminescence [20]. However, OF sensors often lack a sufficiently high sensitivity (S), and their measurable range of variations is limited. Moreover, OFs are susceptible to aging. As for electrical sensors, Liu *et al.* proposed a carbon fiber bending sensor built on a cascade structure, in which a humanoid robot can recognize the extent of joint rotation along with the muscle strain by reading the result of the measurement resistance [21]. However, calibration complexity and high costs are common issues faced by such electrical sensors. These limitations might be addressed by introducing flexible MSs into the design. Zhao *et al.* introduced a flexible terahertz MS by extracting a resonance state in a multi-band as a curvature detection object, where the bending strain of the structure induces a resonance frequency shift as well as an enhancement of the resonance strength [22]. The sensing range and S in this work are relatively limited compared to fiber optic sensors. As of now, the exploration of curvature sensing based on flexible MSs or OMs is still relatively nascent.

In contrast to preceding studies on curvature sensing, this research introduces a flexible substrate, aramid paper (AP), and implements a based liquid crystal (LC) tunable OMS sensing design. Upon application of the OMS onto the measured surface, the absorptivity curve showcases a quadratic trend with increasing object curvature, enabling extensive curvature sensing ranging from 0 to 0.327 mm^{-1}. Notably, it attains a maximum S of 0.918/mm^{-1} and achieves a high quality factor (Q-factor) of 25.88. Concurrently, the incorporation of LC introduces tunability to the OMS through a bias voltage. In the bias state, the sensing performance of the OMS experiences significant augmentation, with S and Q-factor reaching up to 1.333/mm^{-1} and 27.60, respectively.

2. Theory and configuration

Figure 1 presents a three-dimensional schematic illustration of the OMS, structured as a classical sandwich design encompassing a resonant copper ring, an upper AP layer, LC, a copper film, and a bottom AP layer. The choice of utilizing resonant copper rings is twofold. On one hand, copper rings are easily processed and can be conveniently plated onto AP. On the other hand, adopting

Optics EXPRESS

copper rings as central symmetric resonant structures is advantageous for forming a single absorption peak, facilitating theoretical exploration of the impact of curvature on absorption intensity. This approach aims to minimize potential interference from curvature and other latent effects. The high frequency structure simulator (HFSS) is employed for numerical simulations of the OMS within the frequency band of 4 GHz to 16 GHz. The positive incident plane wave is the y-polarized EMW. The electric field **E** component of the EMW aligns parallel to the + y-direction, while the magnetic field component aligns along the + x-direction. The boundary conditions are defined as the master and slave and are employed to numerically simulate the periodic OMs. The other parameters in Fig. 1(c) are presented in Table 1.

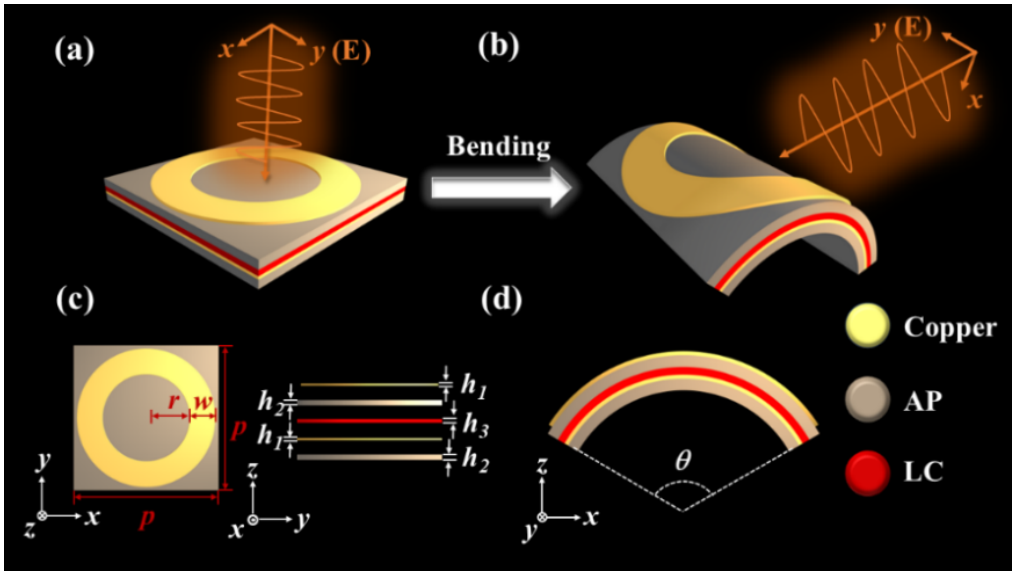

Fig. 1. Schematic diagrams of unit cell for the OMS: (a) Planar schematic diagram of the cell. (b) Schematic diagram of the bending cell. (c) Top view and right view of the cell. (d) Right view of the cell bent in the x-direction.

Table 1. Related parameters of the OMS

p (mm)	r (mm)	w (mm)	h_1 (mm)	h_2 (mm)	h_3 (mm)
8	3	0.8	0.036	0.3	0.1

The absorptivity $A(\omega)$ is derived from Eq. (5), where $R(\omega)$ and $T(\omega)$ signify reflectance and transmission, encompassing both cross-polarized and co-polarized components. Additionally, $R(\omega)$ and $T(\omega)$ can be equivalently expressed by the reflectance coefficients S_{11} and transmission coefficient S_{22}, as detailed in Eqs. (3) and (4). The S-parameters commonly characterize the transmission properties of EMW within the microwave field. Notably, due to the reflective nature of the copper film on the bottom AP, the contribution of S_{21} can be deemed negligible. Consequently, the absorptivity can be simplified as $A(\omega) = 1\text{-}\ S_{11}{}^2$.

$$T(\omega) = |t(\omega)_{yy}|^2 + |t(\omega)_{xy}|^2 \tag{1}$$

$$R(\omega) = |r(\omega)_{yy}|^2 + |r(\omega)_{xy}|^2 \tag{2}$$

$$T(\omega) = S_{21}^2 \tag{3}$$

Optics EXPRESS

$$R(\omega) = S_{11}^2 \tag{4}$$

$$A(\omega) = 1 - R(\omega) - T(\omega) \tag{5}$$

where $t(\omega)_{yy}$, $t(\omega)_{xy}$, $r(\omega)_{xy}$ and $r(\omega)_{xy}$ represent the co-polarized transmittance, cross-polarized transmittance, co-polarized reflectance, and cross-polarized reflectance, respectively. The resonance pattern is a toroidal copper film with a conductivity of 5.8×10^7 S/m [23]. The AP employed for this structure is G-Flex meta-aramid paper YT510 [24]. The dielectric constant of AP is 2.9 [24], with a dielectric loss factor, *i.e.*, loss angle tangent, of 0.007 [24], enabling the OMS to absorb a certain amount of EMW input signal. As the absorbed signals are utilized as detection signals, the detection process does not cause substantial damage to the MMS. Furthermore, since the LC is encapsulated between two layers of AP and shielded by the AP layers, it is not directly exposed to the external environment. Therefore, the durability of this structure primarily depends on the AP. The AP, being a common industrial material, possesses good corrosion and heat resistance, with their dielectric parameters minimally affected by the environment [25]. The AP layers serve as a paper-based material replacing traditional glass dielectric substrates. Its primary function lies in encapsulating and securing the LC, while also possessing a certain degree of flexibility to conform to curved surfaces.

Nematic phase LC is introduced between two layers of Aps. LC, as a type of fluid material, actually exhibits a certain viscosity [26]. This implies that the thickness of the sealed LC layer will not undergo significant changes with increasing curvature at the appropriate temperature. In traditional flexible LC displays, there are often locally uneven portions within the LC layer. Theoretically, these uneven parts can be addressed by adding ultra-thin spacers between the layers of APs. In theory, as long as the dielectric parameters of the selected ultra-thin spacers match the equivalent dielectric parameters of the LC, the resulting impact would be minimal. LCs are categorized as uniaxially anisotropic materials, wherein the molecules director align along the direction of the optical axis [27]. The director is controlled by the applied voltage. In the absence of voltage, the nematic LC molecules align uniformly, allowing the molecular director to easily align along the flow direction due to external force. As illustrated in Fig. 2(a), the horizontal alignment of the director along the + x-direction is typically achieved through rubbing alignment. At this point the OMS is in the initial state, with its dielectric constant tensor expressed by the following Eq. (6) [28]:

$$\varepsilon = \begin{pmatrix} \varepsilon_{\parallel} & 0 & 0 \\ 0 & \varepsilon_{\perp} & 0 \\ 0 & 0 & \varepsilon_{\perp} \end{pmatrix} \tag{6}$$

where $\varepsilon_{||}$ signifies the dielectric constant pertaining to the **E** aligned parallel to the LC director, and $\varepsilon_{\perp}$ denotes the dielectric constant when **E** is perpendicular to the director. When an external voltage is applied between the copper resonant mode and the copper mirror, the LC director will realign, as depicted in Fig. 2(b). Upon reaching the saturation voltage, the director aligns itself along the z-direction. At this juncture, the OMS is in the bias state, the dielectric constant tensor, as denoted ε' by Eq. (7).

$$\varepsilon' = \begin{pmatrix} \varepsilon_{\perp} & 0 & 0 \\ 0 & \varepsilon_{\perp} & 0 \\ 0 & 0 & \varepsilon_{\parallel} \end{pmatrix} \tag{7}$$

Nematic phase LCs exhibit dichroism as an anisotropic material, *i.e.*, $\tan \delta_o \neq \tan \delta_e$. It suggests that the effective loss of LC is not fixed but rather subject to modification within a specific range through external stimuli. This mechanism precisely illustrates the operational principle behind electrically tune LC devices. The LC employed in this work is K15 (5CB) [27]. When

Optics EXPRESS

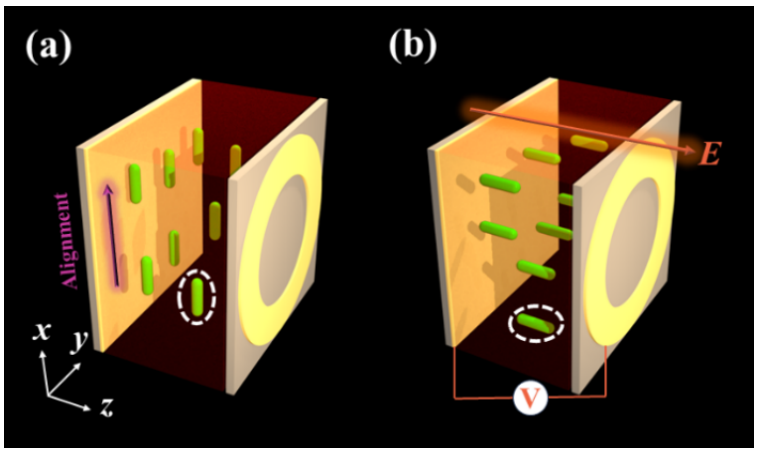

Fig. 2. The LC director (a) in the initial state; (b) in the bias state.

functioning within the frequency span of 0.36 GHz to 23 GHz, the relative dielectric constants are $\varepsilon_{\perp} = 2.6$ and $\varepsilon_{||} = 2.77$ [27], while the loss angle tangent is $\tan\delta_{\perp} = 0.022$ and $\tan\delta_{||} = 0.042$ [27]. The LC, being a fluidic material, is encapsulated within the AP layers and experiences the force exerted by the APs, which also undergoes bending. The primary contribution of LC lies in its electrically tunable performance. By applying voltage, its absorption state can be adjusted, transitioning from the initial state to the bias state. In situations deviating from room temperature, due to the temperature sensitivity of the LC, applying a saturated voltage to the superstructure biases it, thereby mitigating the effects induced by temperature and enhancing sensing capabilities. Moreover, the stability of the metastructure mainly hinges on the dielectric parameters of the various materials, which are minimally affected by the environment in the case of aramid paper and copper. The only caveat is that the K15(5CB) itself is sensitive to temperature [29], potentially leading to slight variations in its dielectric constant if the temperature deviates from room temperature. Consequently, a bias voltage is applied to the MS to maintain the LC's dielectric parameters at a fixed value, thus reflecting the tunability of the MS.

3. Adsorption mechanism and sensing performance

3.1. Phenomena and results

In Fig. 3, absorptivity is computed at $\theta = 0°$, 30°, 60°, 90°, 120°, and 150°, elucidating the distinct electromagnetic absorption characteristics exhibited by the absorber at different θ. Upon incrementing θ from 0° to 150° in 30° intervals, there is a slight shift in the resonant frequency of the OMS, from 10.24 GHz to 10.144 GHz. Additionally, in Fig. 3(b), the absorptivity escalates from 0.773 to 0.920. The alteration in the peak functions as the measuring signal of the bending degree and bending curvature (K). The bending action notably enhances the absorption performance of the OMS. This mechanism enables OMS to achieve detection capability.

Figs. 4(a) and (b) scrutinize the absorption amplitude distribution under varying degrees of bending. The distribution of amplitude distinctly is predominantly concentrated around 10 GHz. Moreover, the energy absorption amplitude in proximity to the central frequency gradually strengthens with the enlargement of θ (see Fig. 1). The variations in absorption amplitude becomes notably more pronounced in the bias state. To investigate the slight shift in resonance frequency and the gradient of absorption amplitude induced by the bending structure, the absorptivity peak and center frequency are meticulously recorded at 5° intervals as θ ascends from 0° to 150°. The findings presented in Figs. 4(c) and (d) reveal the consistent stability of

Optics EXPRESS

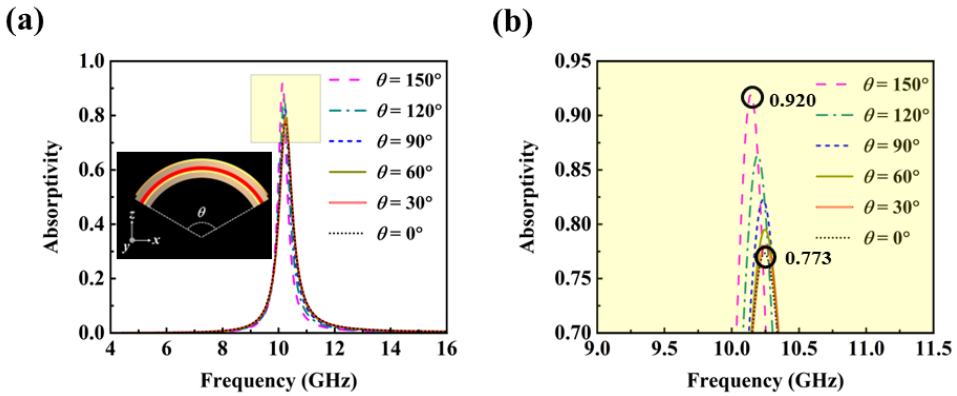

Fig. 3. (a) The absorptivity of the OMS at different θ. (b) Partially zoomed view in (a) (yellow area).

the center frequency at 10.252 GHz within the range of 5° to 60°. This phenomenon suggests the prospective application of OMS for single frequency point signal sensors. Additionally, the absorptivity curve exhibits an upward trajectory with a quadratic variation, $A_p = 7.063 \times 10^{-6}\theta^2$-$1.158 \times 10^{-4}\theta$+0.776, $R^2 = 0.9992$, as portrayed in Fig. 4(c). In the bias state, the resonant frequency stabilizes within the angle range of 5° to 85°, representing a 25° increment from the initial state. This broadening of the θ range signifies a considerable enhancement in the operational scope. In the bias state, the fitted curve shifts significantly downward, $A_p = 1.018 \times 10^{-5}\theta^2$-$1.439 \times 10^{-4}\theta$+0.659, $R^2 = 0.9996$, while the gradient of the variation of the absorption amplitude becomes larger. The alteration in the slope of the curve further demonstrates that the introduction of LC is feasible for tunable OMS. Additionally, given that the skin depth of metallic copper at 10 GHz is 0.66 nm, considerably thinner than the thickness of the copper film ($h_1 = 0.036$ mm), EMWs are unable to penetrate the OMS. This guarantees the effectiveness of the sensing structure in acquiring signals.

3.2. Sensing performance

To assess the sensing capabilities of the OMS, the key parameters associated with sensor, crucial sensor parameters, specifically, S and the Q-factor which are individually computed for two states. The sensitivity S is defined as the ratio between the change in the output signal and the change in the input signal when the sensor operates in a steady state. This relationship can be approximated by the differentiation $\partial A_p/\partial\theta$ of the fitted curve A_p, as outlined in Eq.(9). In Fig. 5(a), the linear correlation between S and θ is depicted by the straight lines $S = 1.413 \times 10^{-5}\theta$ -1.158×10^{-4} and $S = 2.036 \times 10^{-5}\theta$ -1.439×10^{-4}, corresponding to the two distinct states.

$$S = \frac{\Delta A_p}{\Delta\theta} \approx \frac{\partial A_p}{\partial\theta} \tag{9}$$

$$Q = f/FWHM \tag{10}$$

For MS sensors, the Q-factor serves as a crucial parameter for characterization. It is determined by the Eq.(10), where f represents the center frequency of the absorptivity peak, and FWHM denotes the half-peak full width [30]. The Q-factor are computed for $\theta = 0°$, 30°, 60°, 90°, 120°, and 150°, depicted in Fig. 5(b). There is a notable increase in Q-factor corresponding to the rise in θ. Following voltage regulation, the Q-factor curve experiences a significant upward shift, reaching 25.88 at $\theta = 150°$, while achieving a peak of 27.60 in the bias state. The figure illustrates a noticeable upward shift in the Q-factor curve in the bias state, notably with an approximate

Optics EXPRESS

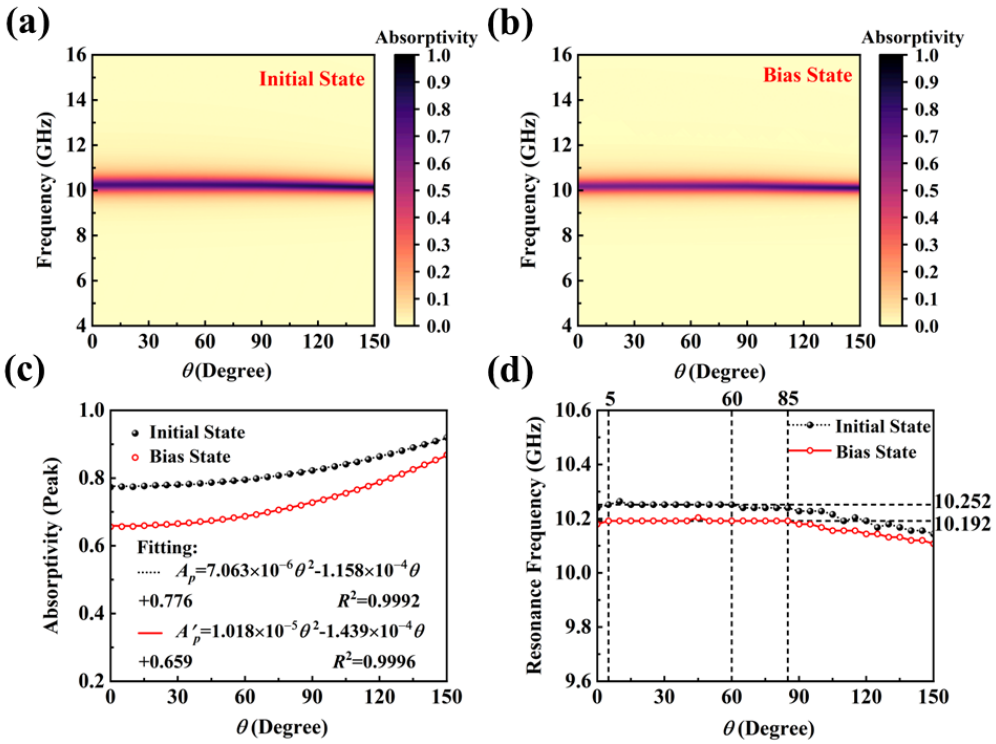

Fig. 4. (a) and (b) Absorbed energy profiles in two states. (c) Variations in absorptivity with respect to θ, from 0° to 150°, recorded in steps of 5°. (d) The offset of the resonant frequency with the change of θ.

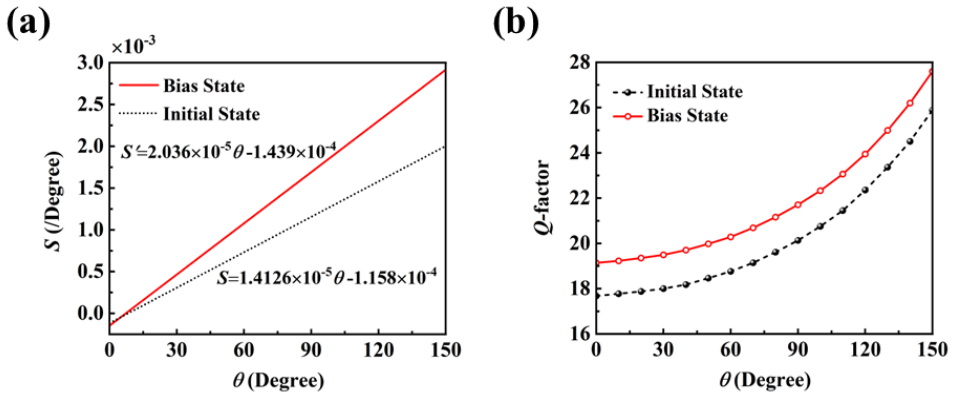

Fig. 5. (a) The S-θ relationship of the OMS. (b) The Q-factor curves of the OMS.

offset of 2. This observed enhancement in sensing performance aligns with the earlier discussion on S.

Degree of bending in the object is commonly characterized by curvature K as indicated in Eq.(11), where R represents the curvature radius. In accordance with the arc length equation presented in Eq.(12) [31], K maintains a linear association with θ, suggesting that the OMS can be effectively converted into a CS. In the curvature detection state, the sensitivity is denoted as

Optics EXPRESS

S_K.

$$K = 1/R \tag{11}$$

$$\frac{\theta}{360^\circ} \times 2\pi R = p \tag{12}$$

where p and θ denote the OMS length, and bending angle, respectively. Figure 6(a) delineates the relationship between absorptivity The ascertainable range for detectable curvature spans from 0 to 0.327 mm^{-1}. Figure 6(b) demonstrates the linear relationship between sensitivity and curvature for two states, $S_K = 2.968K$-0.053 and $S'_K = 4.279K$-0.066, respectively. The maximum of S_K is 0.918 and 1.333, respectively. The results suggest that OMS demonstrates notable sensing capabilities in curvature detection applications. Alongside its wide detection range, the S can be further heightened in the bias state.

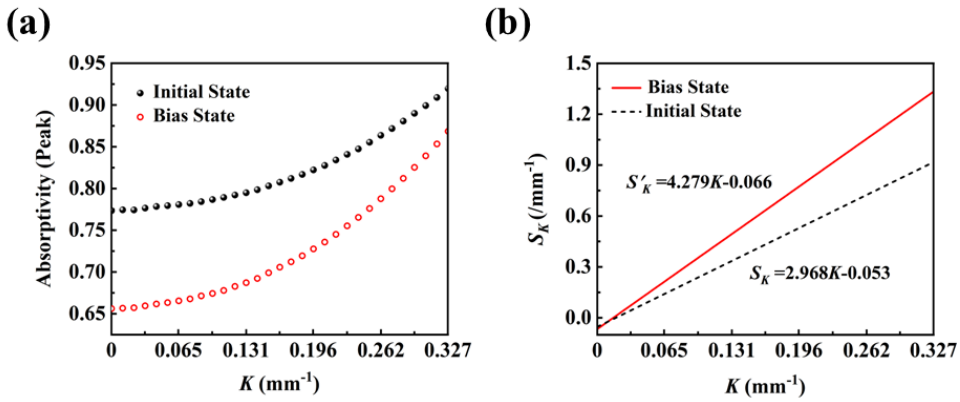

Fig. 6. (a) The absorptivity of the OMS for CSs in two states. (b) The S-K relations of the OMS for CS.

Table 2 delineates the sensing principles and associated metrics of various CSs, offering a comprehensive overview of different sensor types. Previous investigations into CSs have uncovered a scarcity of specialized research specifically focused on sensors based on OMS. The given CS, introduced in this paper, harnesses the absorption principle of electromagnetic absorbers and integrates a flexible MS approach. In comparison to CS designs predominantly relying on OFs and electronic sensors, this innovative approach notably excels in both detection range and S. The detection range, represented by K, spans from 0 to 0.327 mm^{-1}, achieving a maximum S_K of 1.333/mm^{-1}.

3.3. Physical mechanism analysis

To explore the fundamental physical mechanism of the OMS across varying degrees of bending (see Fig. 7(a)), Figs. 7(b) and (c) depict the current distributions respectively observed on the surface of the copper ring and on the lower surface of the LC at θ=0° and 90°. In the initial state, the resonant frequencies are 10.288 GHz and 10.240 GHz, respectively. In Fig. 7(b), electric current courses from one pole to another, chiefly accumulating along the inner edge proximate to the equatorial line within the copper ring. This flow exhibits symmetry along the central -y-axis direction. At θ=90° within the ring, there is a pronounced accumulation of current compared to the position at θ=0°. Moreover, a fraction of the current circulates along the outer periphery of the ring, exhibiting a trajectory identical to that observed along the inner edge. The concentration of currents near the equatorial periphery is interpreted as negative charges, while those in the proximity of the poles are designated as positive charges. These charges result in the formation of a symmetrically distributed arc **E** along both the inner and outer edges of the copper film,

Optics EXPRESS

Table 2. Performance of various CSs

Refs.	Material	Principle	Range	Sensitivity	Size	Linearity
[32]	OFs	integration with GaN optoelectronics	30~90°	None	$2.5 \times 1.5 mm^2$	None
[19]	multicore fiber	Fabry-Pérot cavities	0~6.4 m^{-1}	400 pm/m^{-1}	None	None
[11]	OFs	multimode fiber MZI	0~2.36 m^{-1}	-78.75 dB/m^{-1}	$L = 3mm$	None
[33]	OFs	polarization characteristics	0~0.15 m^{-1}	12.26/m^{-1}	$160 \times 25 \times 6$ mm	0.9949
[34]	OFs	FBG	0.035~0.055mm^{-1}	35.3426 nm/m^{-1}	$H = 4.33$ mm	None
This work	AP	Electromagnetic absorber	0~0.327mm^{-1}	1.333/mm^{-1}	$8 \times 8 \times 0.772$ mm	0.9997

as depicted in Fig. 7(d). The current distribution on the lower surface of the LC layer closely resembles that observed on the surface of the copper ring in Fig. 7(c). However, a notable distinction lies in the opposite direction of the current flow. Therefore, the interaction of two opposing parallel currents generates a resonant circulating loop between the upper and lower surfaces, ultimately initiating a magnetic resonance.

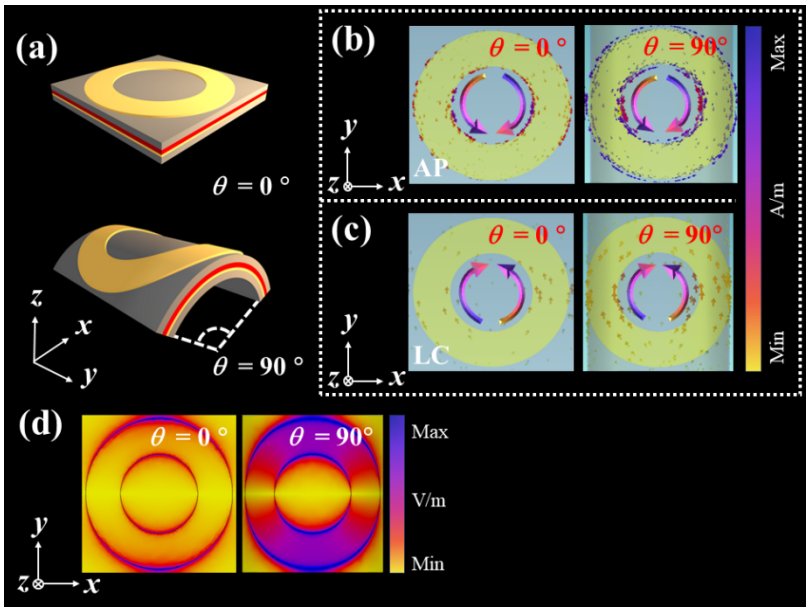

Fig. 7. Current distribution and near **E** distribution. (a) Views of the OMS at θ=0° and 90°, with resonant frequencies corresponding to 10.288 GHz and 10.240 GHz, respectively. (b) Current distribution on the upper surface. (c) Current distribution on the lower surface of the LC. (d) Near **E** distribution of the OMS surface.

In the initial state, the results in Fig. 8 are conducted to investigate the density distribution of energy loss in the AP and LC layers. The analysis presented in Figs. 8(a) and (b) reveals energy losses occurring in both AP and LC layers. Moreover, a considerable amount of energy loss is evident in the substrate AP, whereas the thinner LC layer, characterized by thickness h_3 (see Fig. 1), exhibits relatively lower incident EMW energy loss. This dielectric loss can be explained

Optics EXPRESS

by the fact that the **E** component of an EMW incurs losses during propagation through a medium due to hysteresis effects induced by conductivity and polarization. Additionally, variations in the degree of curvature within the same medium induces differing levels of medium losses. When $\theta = 90°$, as depicted by the circles in Fig. 8, the energy within the loss region intensifies. This phenomenon has also been observed in [27], but the specific mechanism governing its generation has not been explicitly outlined.

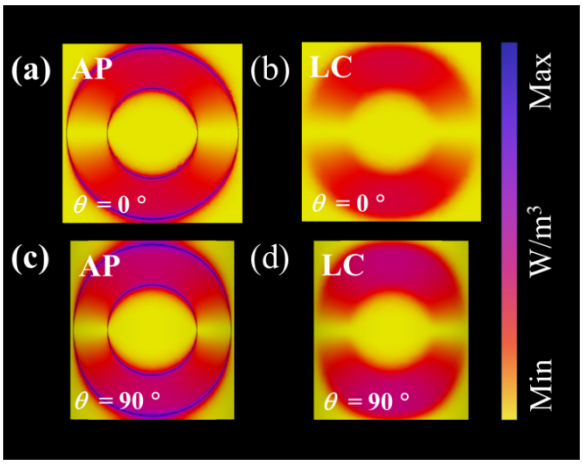

Fig. 8. Energy loss density map. (a) and (c) are the energy loss distribution of the AP, respectively, and (b) and (d) are the energy loss distribution of the LC, respectively.

The absorption of incident EMWs can be elucidated through the theories of magnetic resonance, dielectric loss, and interference theory [35]. In Fig. 7(b), the near **E** distribution in the vicinity of the copper ring experiences local enhancement at $\theta = 90°$. This enhanced region aligns with where the planar structure generates an equivalent **E** distribution. This phenomenon be explained by the curvature induced effect [36–38]. The curvature induced effect arises from the system's curvature, introducing an additional contribution of effective energy. This additional energy is commonly known as the geometric potential. Building upon the prior analysis, a magnetic resonance occurs between the upper and lower surfaces [39], generating an equivalent surface charge before the structure bends. Post-bending, the material can segregate into geometric and tangential charges aligned along the magnetization direction. Geometric charges arise from curvature induced effects, while tangential charges correspond to the equivalent charges observed in planar structures [40]. The existence of geometric charges leads to additional potential energy, and Fig. 7(d) demonstrates the localized field enhancement apparent in the structure's bent state. Furthermore, this geometric potential is corroborated by the energy loss densities depicted in Figs. 8(a) and (c). Upon the OMS's bending, the energy loss density distribution notably intensifies owing to the presence of this geometric charge, thereby significantly enhancing the resonance absorptivity.

4. Parameter optimization and discussion

The fabrication of OMS can be accomplished by microfabrication techniques, including photolithography [32], and inkjet printing [41]. However, these processes inevitably generate errors in the detection results. The outcomes of numerically optimizing the parameters indicate that variations in the radius (r), width (w) of the resonant copper ring, and AP thickness (h_2) have a notable impact on the output signal. Figure 9 visually illustrates the absorptivity collected for these parameters within a defined proximity range. The impact of h_2 on sensing performance is

Optics EXPRESS

depicted in Fig. 9(a), illustrating variations ranging from 0.28 mm to 0.32 mm at intervals of 0.01 mm. The figure distinctly illustrates a noticeable downward shift in the overall curve with an increase in h_2. Thus, it is only necessary to recalibrate the output to account for the actual h_2 change. This recalibration process does not significantly affect the linearity and range of the detection results.

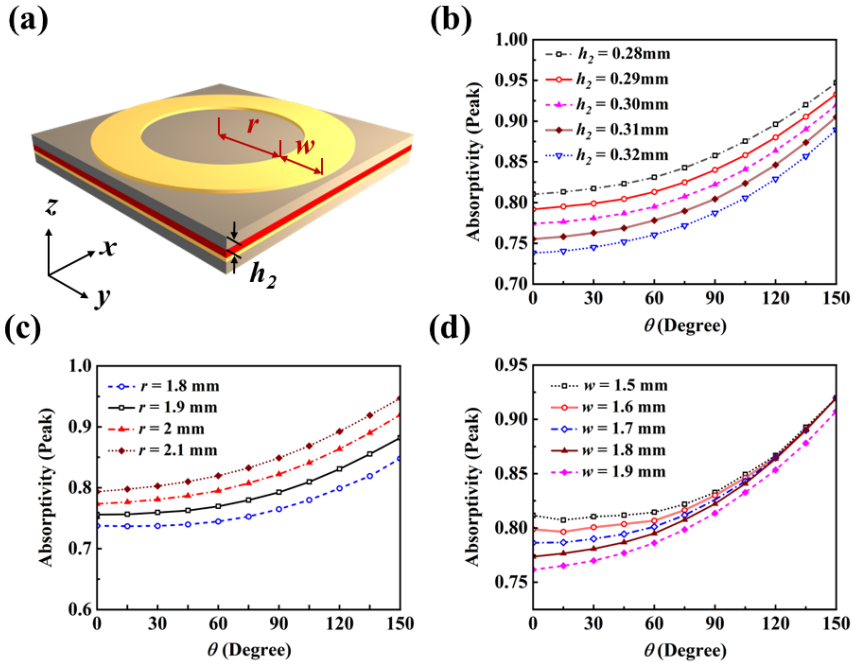

Fig. 9. (a) Sizes of the OMS unit. Influences of (b) the AP thickness; (c) the width of the resonant copper ring; (d) the radius of the resonant copper ring.

The impact of w on absorption amplitude is investigated in Fig. 9(c), while maintaining $h_2 = 0.3$ mm and $r = 2$ mm, respectively. As w increases, a noticeable rising concave trend emerges in the absorptivity curve. The deviation disrupts the sensor's linearity and S, particularly evident at $w = 1$ mm, where the absorptivity curve takes on a concave shape, leading to inaccurate detection signals. To maintain stability within the sensing system, it becomes crucial to minimize the occurrence of such errors and aim to sustain $w = 1.8$ mm. Figure 9(d) demonstrates a progressive upward concavity in the curve as θ increases, accompanying a reduction in the radius r from 1.8 mm to 2.1 mm. Consequently, the S no longer exhibits linear variation, significantly compromising the sensor's capability. To ensure accurate detection, maintaining a near-perfect r close to 2 mm becomes imperative, necessitating precision in machining processes.

The prior analysis underscores three critical errors that significantly influence the outcomes. Optimal parameters which are $r = 2$ mm, $h_2 = 0.3$ mm, and $w = 1.8$ mm, have been established. However, owing to limitations imposed by the practical working environment, achieving a perfectly positive incidence of the EMW as the driving energy is challenging. Hence, a comprehensive discussion on the errors stemming from the incidence angle (θ_I) is necessary (see Fig. 10(a)). In Fig. 10(b), five cases are depicted with θ_I of 0°, 10°, 20°, 30°, and 40°. At $\theta_I = 10°$, a slight upward shift is observed in the curve, while S shows minimal change. However, deviations of 20°, 30°, and 40° from the positive incidence result in a notable upward shift in absorptivity curve. This generalized rise in absorptivity signals a departure from the expected output signal

Optics EXPRESS

concerning A_p. Such deterioration disrupts the detectability of the OMS. To preserve the sensor's precision, it is crucial to confine θ_I within a 5° range.

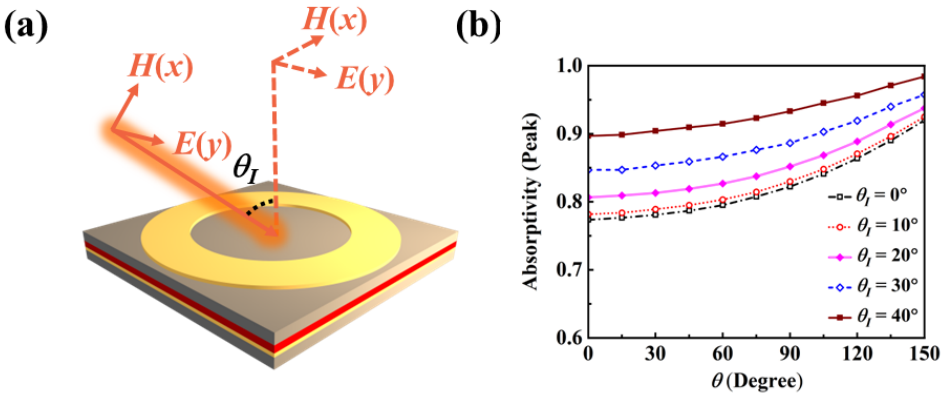

Fig. 10. (a) Schematic of incident wave deviation from normal incidence. (b)The influence of θ_I on absorptivity.

5. Conclusion

In summary, a novel LC-based tunable OMS tailored for curvature sensing is presented. The OMS demonstrates a broad curvature sensing ranges from 0 to 0.327 mm^{-1}, achieving a maximum S of 0.918/mm^{-1} and a notable Q-factor of 25.88. Incorporating a tunable LC layer significantly enhances operational performance through voltage adjustments, optimizing sensitivity up to a maximum of 1.333/mm^{-1} and the Q-factor up to 27.60. This investigation delves into the potential application of the OMS in curvature sensing, contributing to the advancement of CS design paradigms. These findings open avenues for further developments in fields like bionic robotics and electronic skin.The OMA is expected to be integrated into photonic chips for detecting deformations and variations in the chip, enabling real-time monitoring and optimization of the performance and stability of the photonic chip. Additionally, the OMA, with its curvature sensing capability, holds promise for applications in medical photonic systems, allowing for real-time monitoring of joint movements and changes in body morphology for diagnostic and therapeutic purposes.

Funding. Natural Science Research Start-up Foundation of Recruiting Talents of Nanjing University of Posts and Telecommunications (NY222105); Natural Science Foundation of Jiangsu Province, Major Project (BK20212004); National Natural Science Foundation of China (62375141); National Key Research and Development Program of China (2022YFA1405000).

Disclosures. The authors declare no conflicts of interest.

Data availability. Data underlying the results presented in this paper are not publicly available at this time but may be obtained from the authors upon reasonable request.

References

1. H. Liu, H. Zhao, S. Li, *et al.*, "Adhesion-Free Thin-Film-Like Curvature Sensors Integrated on Flexible and Wearable Electronics for Monitoring Bending of Joints and Various Body Gestures," Adv. Mater. Technol. **4**(2), 201800327 (2019).
2. Q. Wang and Y. Liu, "Review of optical fiber bending/curvature sensor," Measurement **130**, 161–176 (2018).
3. R. Kowerdziej, A. Ferraro, D. C. Zografopoulos, *et al.*, "Soft-Matter-Based Hybrid and Active Metamaterials," Adv. Opt. Mater. **10**, 71890 (2022).
4. S. Xu, F. Fan, H. Cao, *et al.*, "Liquid crystal integrated metamaterial for multi-band terahertz linear polarization conversion," Chin. Opt. Lett. **19**(9), 093701 (2021).

Optics EXPRESS

5. J. Shu and Y. Zhang, "Utilizing Metamaterial Characteristic to Enhance the Tunability of Liquid Crystal," *presented at the 2021 IEEE MTT-S International Microwave Workshop Series on Advanced Materials and Processes for RF and THz Applications* (IMWS-AMP)2021.
6. X. Li, G. Zheng, G. Zhang, *et al.*, "Highly Sensitive Terahertz Dielectric Sensor for Liquid Crystal," Symmetry **14**(9), 1820 (2022).
7. R. Melik, E. Unal, N. K. Perkgoz, *et al.*, "Metamaterial-based wireless strain sensors," Appl. Phys. Lett. **95**(1), 011106 (2009).
8. A. I. Aristov, M. Manousidaki, A. Danilov, *et al.*, "3D plasmonic crystal metamaterials for ultra-sensitive biosensing," Sci. Rep. **6**(1), 25380 (2016).
9. M. Bakır, M. Karaaslan, E. Unal, *et al.*, "Microwave metamaterial absorber for sensing applications," Opto-Electron. Rev. **25**(4), 318–325 (2017).
10. G. E. Lio, A. Ferraro, R. Kowerdziej, *et al.*, "Engineering Fano-Resonant Hybrid Metastructures with Ultra-High Sensing Performances," Adv. Opt. Mater. **11**(12), 2203123 (2023).
11. X. Yang, B. Luo, D. Wu, *et al.*, "Highly sensitive curvature sensor based on a sandwich multimode fiber Mach–Zehnder interferometer," Opt. Express **30**(22), 40251–40264 (2022).
12. C. Wang, Z. Lv, M. P. Mohan, *et al.*, "Pangolin-Inspired Stretchable, Microwave-Invisible Metascale," Adv. Mater. **33**(41), 202102131 (2021).
13. Z. Luo, S. Ji, J. Zhao, *et al.*, "An ultra-thin flexible conformal four-band metamaterial absorber applied in S-/C-/X-band," Phys. Scr. **97**(4), 045813 (2022).
14. S. Tomita, K. Shimanuki, S. Oyama, *et al.*, "Transition of deformation modes from bending to auxetic compression in origami-based metamaterials for head protection from impact," Sci. Rep. **13**(1), 12221 (2023).
15. Y. Han, Q. Li, B. Li, *et al.*, "Light-weight wideband electromagnetic wave absorber based on aramid paper," Appl. Phys. Lett. **122**(25), 251702 (2023).
16. D. Xiao, G. Wang, F. Yu, *et al.*, "Optical curvature sensor with high resolution based on in-line fiber Mach-Zehnder interferometer and microwave photonic filter," Opt. Express **30**(4), 5402 (2022).
17. R. Zhao, H. Liu, and X. Shu, "Femtosecond laser-inscribed off-axis high-order mode long-period grating for independent sensing of curvature and temperature," Opt. Express **30**(21), 37697 (2022).
18. Z. Yin, X. Jing, K. Li, *et al.*, "Experimental study of an intensity-modulated curvature sensor with high sensitivity based on microstructured optical fiber," Opt. Express **31**(3), 4770 (2023).
19. R. Oliveira, M. Cardoso, and A. M. Rocha, "Two-dimensional vector bending sensor based on Fabry-Pérot cavities in a multicore fiber," Opt. Express **30**(2), 2230 (2022).
20. W. Xu, Y. Li, J. Shang, *et al.*, "Optical fiber sensor based on upconversion luminescence for synchronous temperature and curvature sensing," Opt. Express **30**(18), 33136–33144 (2022).
21. J. Liu, F. Liao, Z. Chen, *et al.*, "Digitizing Human Motion via Bending Sensors toward Humanoid Robot," Adv. Intell. Syst. **5**, 1110–1113 (2023).
22. X. Zhao, B. Yang, J. Liu, *et al.*, "A multiband flexible terahertz metamaterial with curvature sensing functionality," J. Opt. **18**(7), 075101 (2016).
23. X. Luo, P. Xiang, H. Yu, *et al.*, "Terahertz Metamaterials Broadband Perfect Absorber Based on Molybdenum Disulfide," IEEE Photonics Technol. Lett. **34**(20), 1100–1103 (2022).
24. THE GUND COMPANY. (2023). G -Flex™ YT510. Retrieved from: https://thegundcompany.com/materials-2/flexible-materials/
25. Y. Yao, M. Huang, J. Ma, *et al.*, "Effects of Hot Pressing Temperature and Pressure on Dielectric Properties of Aramid Insulating Paper," Energies **15**(21), 8314 (2022).
26. C. Tadokoro, T. Nihira, and K. Nakano, "Minimization of Friction at Various Speeds Using Autonomous Viscosity Control of Nematic Liquid Crystal," Tribol. Lett. **56**(2), 239–247 (2014).
27. D. C. Zografopoulos, A. Ferraro, and R. Beccherelli, "Liquid-Crystal High-Frequency Microwave Technology: Materials and Characterization," Adv. Mater. Technol. **4**(2), 1800447 (2019).
28. H. Maune, M. Jost, R. Reese, *et al.*, "Microwave Liquid Crystal Technology," Crystals **8**(9), 355 (2018).
29. S. Mueller, A. Penirschke, C. Damm, *et al.*, "Broad-band microwave characterization of liquid crystals using a temperature-controlled coaxial transmission line," IEEE Trans. Microwave Theory Tech. **53**(6), 1937–1945 (2005).
30. L. Zeng and H. F. Zhang, "Absorption Improvement of the Anapole Metastructure for Sensing Applications," IEEE Sens. J. **22**(12), 11644–11652 (2022).
31. K. V. Vineetha, M. Siva Kumar, B. T. P. Madhav, *et al.*, "Flexible and Conformal Metamaterial based Microwave Absorber for WLAN, Wi-MAX and ISM Band Applications," Mater. Technol. **37**(8), 592–609 (2022).
32. F. Shi, H. Zhang, Z. Ye, *et al.*, "Miniature optical fiber curvature sensor via integration with GaN optoelectronics," Comms. Eng. **1**(1), 47 (2022).
33. Y. Su, J. Wang, J. Li, *et al.*, "Optical curvature sensor based on polarization characteristics of optical fiber," Opt. Express **31**(6), 9275 (2023).
34. X. Wang, C. Wu, Y. Wang, *et al.*, "Double Optical Fiber Temperature Compensation Method for Measurement of Interface Pressure Between Simulated Cable and Accessory at High Temperatures," IEEE Trans. Dielectr. Electr. Insul. **30**(3), 1329–1336 (2023).
35. B. X. Wang, C. Xu, G. Duan, *et al.*, "Review of Broadband Metamaterial Absorbers: From Principles, Design Strategies, and Tunable Properties to Functional Applications," Adv. Funct. Mater. **33**(14), 202213818 (2023).

Optics EXPRESS

36. V. Atanasov, R. Dandoloff, and A. Saxena, "Torus in a magnetic field: curvature-induced surface states," J. Phys. A: Math. Theor. **45**(10), 105307 (2012).
37. C. Ortix, S. Kiravittaya, O. G. Schmidt, *et al.*, "Curvature-induced geometric potential in strain-driven nanostructures," Phys. Rev. B **84**(4), 045438 (2011).
38. R. Streubel, P. Fischer, F. Kronast, *et al.*, "Magnetism in curved geometries," J. Phys. D: Appl. Phys. **49**(36), 363001 (2016).
39. M. M. Tirkey and N. Gupta, "Broadband Polarization-Insensitive Inkjet-Printed Conformal Metamaterial Absorber," IEEE Trans. Electromagn. Compat. **63**(6), 1829–1836 (2021).
40. D. D. Sheka, O. V. Pylypovskyi, P. Landeros, *et al.*, "Nonlocal chiral symmetry breaking in curvilinear magnetic shells," Commun. Phys. **3**(1), 128 (2020).
41. R. Zhou, Z. Yu, Z. Wu, *et al.*, "3D printing metamaterials for highly efficient electromagnetic wave absorption," Sci. China Mater. **66**(4), 1283–1312 (2023).